Velocity changes around the Kaikōura earthquake ruptures from ambient noise cross-correlations

Megan Madley, Alexander Yates, Martha Savage, Weiwei Wang, Tomomi Okada, Satoshi Matsumoto, Yoshihisa Iio, Katrina Jacobs

Geophysical Journal International

Geophys. J. Int. (2022) **229,** 1357–1371
Advance Access publication 2021 December 22
GJI Seismology

https://doi.org/10.1093/gji/ggab514

Velocity changes around the Kaikōura earthquake ruptures from ambient noise cross-correlations

Megan Madley [1,2] Alexander Yates [1,3] Martha Savage [1] Weiwei Wang [1] Tomomi Okada [4,5] Satoshi Matsumoto [6] Yoshihisa Iio [7] and Katrina Jacobs [2]

[1] *School of Geography, Environment and Earth Sciences, Victoria University of Wellington, Wellington 6012, New Zealand. E-mail: martha.savage@vuw.ac.nz*
[2] *GNS Science Ltd, Lower Hutt 5011, New Zealand*
[3] *Institut des sciences de la Terre (ISTerre), Université Grenoble Alpes, Université Savoie Mont Blanc, CNRS, IRD, IFSTTAR, 38000 Grenoble, France*
[4] *Graduate School of Science, Faculty of Science, Tohoku University, Sendai 980-8578, Japan*
[5] *International Research Institute of Disaster Science (IRIDeS), Tohoku University, Miyagi 980-0845, Japan*
[6] *Institute of Seismology and Volcanology, Kyushu University, Nagasaki 855-0843, Japan*
[7] *Disaster Prevention Research Institute, Kyoto University, Kyoto 611-0011, Japan*

Accepted 2021 0. Received 2020 October 31; in original form 2021 November 24

SUMMARY

Seismic velocity changes before and after large-magnitude earthquakes carry information about damage present in the surrounding region. This study presents temporal velocity changes detected prior to and following the 2016 November M_w 7.8 Kaikōura earthquake in Canterbury, New Zealand. We use continuous waveform data from 11 short-period seismometers within the Kaikōura region with an average interstation distance of 83 km. Nine-component day-long empirical Green's functions were computed for frequencies between 0.1 and 0.9 Hz for continuous seismic records from 2012 January 1 to 2018 February 28, which also include the 2013 Cook Strait and Lake Grassmere earthquakes. Using the moving-window cross-spectral method, seismic velocity changes were calculated. Immediately following the 2016 Kaikōura earthquake, a decrease in seismic velocity averaged across all component pairs of approximately 0.2 per cent was observed. An increase in seismic velocity of approximately 0.1 per cent after the earthquake was visible over a 1.5 yr period averaged across all component pairs. A depth sensitivity analysis suggests that observed velocity changes were confined to the uppermost 5 km of the subsurface. We consider strong ground motions a likely candidate for the seismic velocity decrease, followed by post-seismic relaxation via crack healing of the faults that ruptured in the Kaikōura region. Fault-zone damage may also have contributed to observed decreases in the vicinity of ruptured faults.

Key words: New Zealand; Seismic noise; Surface waves and free oscillations; Wave propagation; Seismic Interferometry; Coda Waves.

1 INTRODUCTION

Monitoring of crustal properties such as seismic velocities can provide information about regional stresses or subsurface damage. Ambient seismic noise is increasingly being used to understand crustal properties, since cross-correlations of long-duration seismic signals can provide information about the propagation speeds of surface waves (Shapiro & Campillo 2004).

Ambient noise interferometry has been used to successfully detect seismic velocity variations following earthquakes (e.g. Brenguier *et al.* 2008; Nimiya *et al.* 2017; Heckels *et al.* 2018; Civilini *et al.* 2020). The earliest study of earthquake-induced seismic velocity changes recorded using ambient noise cross-correlation was by Wegler & Sens-Schönfelder (2007). They measured a relative seismic velocity decrease of 0.6 per cent following the M_w 6.6 Mid-Niigata earthquake. Another study (Brenguier *et al.* 2008) found velocity changes at Parkfield, recording a velocity decrease of 0.04 per cent following the 2003 M_w 6.5 San Simeon earthquake, and a 0.08 per cent velocity decrease following the 2004 M_w 6.0 Parkfield earthquake. This decrease recovered over several years at the same rate as GPS displacements (Brenguier *et al.* 2008). Since these studies, similar changes have been observed following earthquakes in many countries (e.g Minato *et al.* 2012; Froment *et al.* 2013; Taira *et al.* 2015; Chaves & Schwartz 2016; Nimiya *et al.* 2017; Ikeda & Tsuji 2018; Viens *et al.* 2018), including New Zealand (e.g. Heckels 2017; Yates *et al.* 2019; Civilini *et al.* 2020). Measured changes using ambient noise are often less than 1.0 per cent, though larger decreases have been recorded (e.g. Minato *et al.* 2012; Viens *et al.* 2018). These have been attributed to various factors including co-seismic stress release and damage

caused by strong ground shaking, which can cause cracks to open in the shallow surface and within the fault zone rupture. For a more complete overview of ambient noise interferometry, including monitoring earthquake responses, the recent review by Obermann & Hillers (2019) provides further details.

The M_w 7.8 Kaikōura earthquake on 2016 November 14 is one of the largest earthquakes to have occurred in New Zealand since the 1855 Wairarapa earthquake. Kaikōura is part of the Marlborough Fault System (MFS) in the northeast of the South Island (Fig. 1). The northeastern Marlborough region represents a transition from the oblique continental collision along the Alpine Fault in the south to subduction along the Hikurangi subduction zone in the north (Clark *et al.* 2017).

The 2016 Kaikōura hypocentre was shallow, at 15 km depth, with an epicentre ∼20 km south of the Hope Fault (Hamling *et al.* 2017), near Waiau in North Canterbury (Fig. 1). The earthquake had an oblique thrust mechanism, with the rupture propagating SW to NE in approximately 2 min and terminating offshore in the Cook Strait (Clark *et al.* 2017). From north Canterbury to the Cook Strait (∼150 km), there were surface ruptures on at least 21 separate faults (Litchfield *et al.* 2017; Stirling *et al.* 2017; Fig. 1). There were also surface ruptures offshore (Clark *et al.* 2017).

We report here on the velocity changes in the Kaikōura region over a 6-yr time period that included the 2013 Cook Strait earthquake sequence and the large-magnitude 2016 M_w 7.8 Kaikōura earthquake. A temporary network that was deployed in 2012 was analysed in order to determine the magnitude of velocity changes associated with the earthquakes during this time period.

2 DATA

The data used in this study were acquired using nineteen short period (2 Hz natural period) stations deployed and maintained in the Kaikōura region by the Disaster Prevention Research Institute (DPRI) at Kyoto University (Okada *et al.* 2019; Fig. 1; Supporting Information Table S1). Of the 19 stations and 171 different station pairs available from the short period network, 11 stations and 47 station-pair combinations are used (133 for all component pairs) (Table 1) to establish separation distances ranging from 13 km (CVR–SVR) to 181 km (CCB–SJQ), with an average distance of 83 km. All of these pairs are onshore with azimuth angles ranging from 20° (SJQ–WJM) to 350° (MLF–SRB). The majority of these short-period seismometers have been operating since 2012, with MTV being deployed the earliest, in 2009. Data have been obtained for both horizontal and vertical components. However, quite a few of the stations had component outages due to damage from the 2016 Kaikōura earthquake or due to recording problems. As a result, a few of the stations have missing components for a large duration of the data period (Supporting Information Fig. S1). The duration used in this study covers a 6-yr period from 2012 January 1 to 2018 February 28. This was used to determine if the DPRI stations observed velocity changes from the 2013 Cook Strait, Lake Grassmere and other large-magnitude ($M_w > 5.6$) earthquakes in the Kaikōura region. The final 2 yr (2016 January 1 to 2018 February 28) were examined more closely for velocity changes in the year before and after the November 2016 Kaikōura earthquake.

3 METHODS

Multiple methods exist for measuring velocity perturbations from cross-correlation functions, with a comprehensive comparison between all published methods performed by Yuan *et al.* (2021). The two most common are the stretching technique (Sens-Schönfelder & Wegler 2006) and the Moving-Window Cross-Spectral (MWCS) technique (Poupinet *et al.* 1984; Frechet *et al.* 1989; Clarke *et al.* 2011). We use the MWCS technique here, which compares the cross-spectrum between two stacks of cross-correlations in a series of moving windows. The two stacks consist of a long-duration reference stack, and shorter-duration moving stacks to measure relative velocity changes (Brenguier *et al.* 2008; Clarke *et al.* 2011). Our processing follows four steps: (1) pre-processing raw data, (2) computing cross-correlations, (3) determining moving and reference stacks, and (4) determining velocity changes from relative travel time measurements.

3.1 Pre-processing raw data

Pre-processing of the raw data aims to enhance ambient noise signals and suppress transient signals, such as earthquakes, to maximise the surface wave energy for estimated Green's functions (Bensen *et al.* 2007). Removal of any daily files which had gaps in recordings and instrumental errors was also crucial, as these can result in misleading velocity changes (e.g. Civilini 2018).

MSNoise, a python package developed by Lecocq *et al.* (2014), was used to determine velocity changes from raw seismic data. Raw input consisted of continuous seismic day-long files. An instrument correction was not necessary as we are only working with the DPRI stations and the instrument responses of these stations are identical. Supporting Information Tables S3 and S4 summarize all the parameters used in the processing.

To pre-process the data, first, the raw continuous waveform data are split into 1-d traces and the mean and trend removed. A bandpass is then applied between 0.01–1.2 Hz and data are downsampled to 20 Hz. This filter range was developed from spectrogram plots (see Supporting Information Fig. S2 for an example) and is discussed further in Kortink (2020). Time-domain normalization and frequency normalization are then applied to each trace. We use the nonlinear time domain one-bit normalization (e.g. Brenguier *et al.* 2007; Mordret *et al.* 2013; Savage *et al.* 2013), whereby all positive amplitudes are given the value of 1 and all negative amplitudes are given the value of −1. It is aggressive, but particularly useful for data sets that contain aftershock sequences because small aftershocks can interfere with signals normalised using the RMS method (Heckels *et al.* 2018). Frequency domain normalization through spectral whitening acts to broaden the band of ambient noise signal in cross-correlations and also combats degradation caused by persistent monochromatic sources (Bensen *et al.* 2007). Following time domain normalization, we apply spectral whitening between 0.1–0.9 Hz.

Before the computation of the cross-correlation functions (CCF), horizontal component waveforms are usually rotated from north and east orientations to produce radial and transverse components. For many stations, we did not have enough component data for each station to perform an accurate rotation (Supporting Information Fig. S1), so they have been left as east, north, and vertical components. Day files were visually assessed for quality to ensure that different components were of similar amplitude and that there were no unnatural aspects to the waveform.

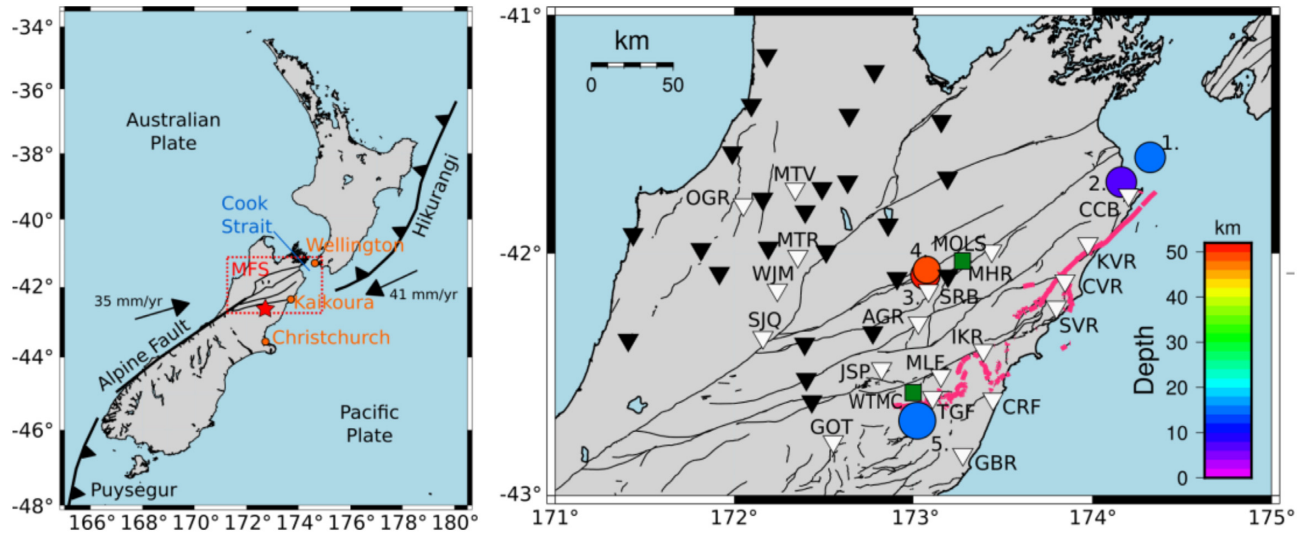

Figure 1. New Zealand map and location of the DPRI stations. Left: the plate boundary with the Pacific and Australian plates shown by the black line with the convergence rates as black arrows. The location of the Marlborough Fault System (MFS) and the region used on the right is shown by the red dashed box. The epicentre of the 2016 Kaikōura earthquake is shown by the red star. Right: the DPRI stations used in this study are shown by the white triangles (see Supporting Information Table S1 for detailed locations). The remaining stations are shown by the black triangles. The two green squares (MOLS and WTMC) are the GeoNet strong motion sites used for PGV analysis. Large-magnitude earthquakes are shown by circles, sized by magnitude and coloured by depth GNS Science: 1—2013 M_w 6.5 Cook Strait; 2—2013 M_w 6.6 Lake Grassmere; 3—2015 M_w 6.2; 4—2016 M_w 5.7; 5—2016 M_w 7.8 Kaikōura (more details can be found in Supporting Information Table S2). Faults that ruptured during the 2016 Kaikōura earthquake are shown by the pink lines (Litchfield *et al.* 2017). Other mapped faults are shown in black (Langridge *et al.* 2016).

Table 1. Relative velocity decreases measured for each component-pair (shown in Fig. 5) following the Kaikōura earthquake. Velocity changes between two time periods are measured as the difference in the average $\delta v/v$ measured within two 10-d time windows. For the co-seismic change a window from 2016 November 2 to 12 is used for pre-earthquake velocity and a window from 2016 December 14 to 24 for post-earthquake velocity (demonstrated in Supporting Information Fig. S7). The delayed measurement of the second window accounts for the 30-d stack size, where 2016 December 14 is the first measurement consisting only of cross-correlation functions produced using post-earthquake data. For the post-seismic change, we use a window from 2018 February 15 to 25 and compare with the measurement window immediately following the earthquake. Errors are calculated based on the minimum and maximum velocity that can be resolved when taking into account measurements error within the 10-d time windows.

Component	Stations used	No. of pairs	Avg. interstation distance (km)	Co-seismic $\delta v/v$ (per cent)	Post-seismic $\delta v/v$ (per cent)
EE	CVR, IKR, JSP, KVR, MLF, MTV, SJQ, WJM	28	85	−0.17±0.09	0.1±0.09
EN	JSP, MLF, SJQ, WJM	6	56	−0.18±0.07	0.08±0.09
EZ	CVR, IKR, JSP, MLF, SJQ, WJM	15	73	−0.21±0.08	0.03±0.09
NE	JSP, MLF, SJQ, WJM	6	56	−0.28±0.06	0.12±0.08
NN	CCB, JSP, MLF, SJQ, SVR, WJM	15	95	−0.16±0.09	0.04±0.1
NZ	JSP, MLF, SJQ, SVR, WJM	10	75	−0.18±0.08	0.02±0.09
ZE	CVR, IKR, JSP, MLF, SJQ, WJM	15	73	−0.20±0.08	0.04±0.1
ZN	JSP, MLF, SJQ, SVR, WJM	10	75	−0.16±0.08	0.05±0.09
ZZ	CVR, IKR, JSP, MLF, SJQ, SRB, SVR, WJM	28	70	−0.23±0.09	0.15±0.11

3.2 Computing cross-correlations

Following pre-processing, the daily traces are cross-correlated. For each station pair where data is recorded for both stations for the whole day, each component of one is cross-correlated with the components of the other. This produces nine different horizontal and vertical component combinations: EE, EZ, EN, NE, NN, NZ, ZE, ZN, ZZ, where E, N and Z represent east, north and vertical components respectively. These component pairs give an approximation of the nine-component Green's tensor. To produce daily cross-correlation functions, signals are cross-correlated in short time windows (1800 s; see supplemental material) and then linear stacking is applied, so that the daily CCF is the mean of the CCF of all windows in the day.

3.3 Moving and reference stacks

Cross-correlation functions are stacked to improve the signal-to-noise ratio (SNR) and therefore the temporal stability (Bensen *et al.* 2007). The purpose behind stacking is to enhance coherent energy. While this is often achieved by stacking more days together, small velocity changes occurring over a short time period can be increasingly difficult to recover. Care must therefore be taken when choosing the moving stack size, with thought given to the temporal resolution of anticipated changes. Further, the moving stacks should be of short duration compared to a reference stack of longer duration.

To determine if coherent energy was visible at different stack sizes, plots like Fig. 2 were generated for each station pair. Ambient noise cross-correlations are usually composed of direct body and

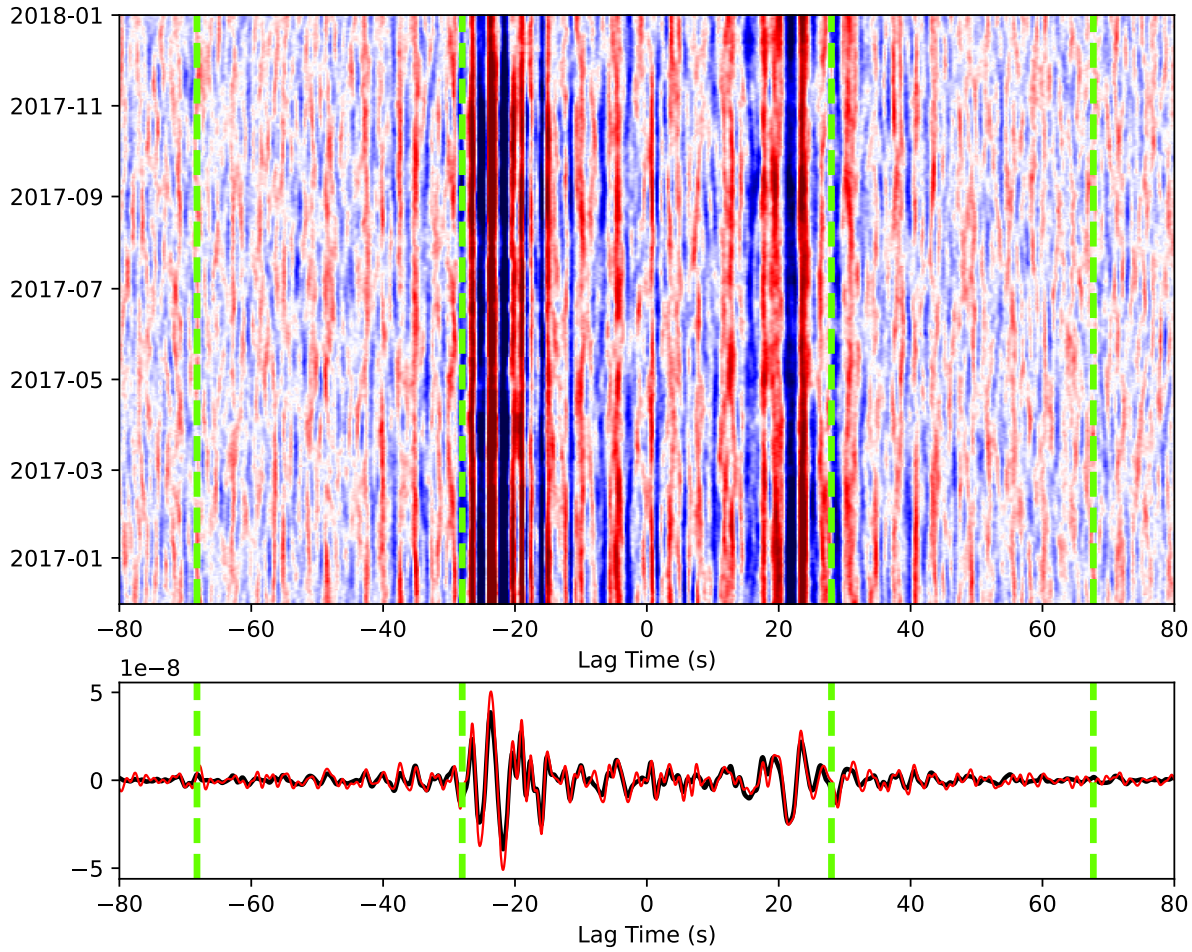

Figure 2. Interferogram plot for the vertical–vertical components of station pair JSP–SJQ with an interstation distance of 56 km. Green dashed bars indicate the coda windows for this station pair. Above: interferogram plot for 30-d stacks for just over 1 yr with red showing positive amplitude and blue showing negative amplitude. Below: waveform of cross-correlations with the black line showing the reference stack and the red line showing the daily cross-correlation on 2016 December 1.

surface wave arrivals and coda waves, which corresponds to waves that have been scattered at least once on their way from one station to another (Hobiger *et al.* 2012). A dynamic coda window (shown in green in Fig. 2) was chosen to begin at the arrival time of waves travelling 2 km s^{-1} between each station pair, with the window lasting for 40 s. This left out the direct waves. Coda waves are ideal for measuring changes in seismic velocity as they can accumulate more delay and are less sensitive to changes in noise source than direct waves (Hadziioannou *et al.* 2011).

Reference stacks of cross-correlations are shown in Fig. 3 against interstation distance for the entire 6-yr data set. As the energy travels between stations, direct arrivals occur at increasingly later lag times as the interstation distance increases. Peaks in arrival times for the nine component pairs generally follow the same trends. However, the clearest direct arrivals are observed in the cross-correlations where the same component is used at both stations (ZZ, EE and NN). Component pairs that include the north component are less clearly resolved. This figure also shows that by choosing a dynamic lag time (shown by the grey transparent box) most of the direct arrivals are excluded for the processing.

Choosing the reference stack length is an important parameter choice. The reference stack should represent the background state of the cross-correlation function. As such, the reference stack should always be longer (contain more days) than the moving stack. To examine the impact of the length of the reference stack, the final 2 yr of the data set was tested to determine how velocity changes were affected by a reference period of 6 months well before the earthquake (2016 January 1 to July 1) or a reference period using the entire 2-yr period, which includes the earthquake and surrounding times (2016 January 1 to 2018 January 1) (Supporting Information Fig. S3). For a variety of different moving windows, the velocity change values associated with the earthquake are larger using the 2-yr than the 6-month reference period. For all of the moving windows, the longer reference period of 2 yr produced smoother velocity variations while also showing a clear decrease after the Kaikōura earthquake. Due to the advantages of the longer reference stack, for the full data set we choose to use the entire 6 yr as a reference period.

Different moving stack sizes were tested as part of this study (5, 10, 20, 30, 60 and 90 d). To determine an appropriate size, we examined how clearly velocity changes were resolved and the correlation coefficients values recorded when compared to the reference stack (Supporting Information Figs S3–S5). From this process we determined that a moving stack of 30 d and a minimum of 0.8 correlation coefficient was effective to demonstrate clear velocity changes.

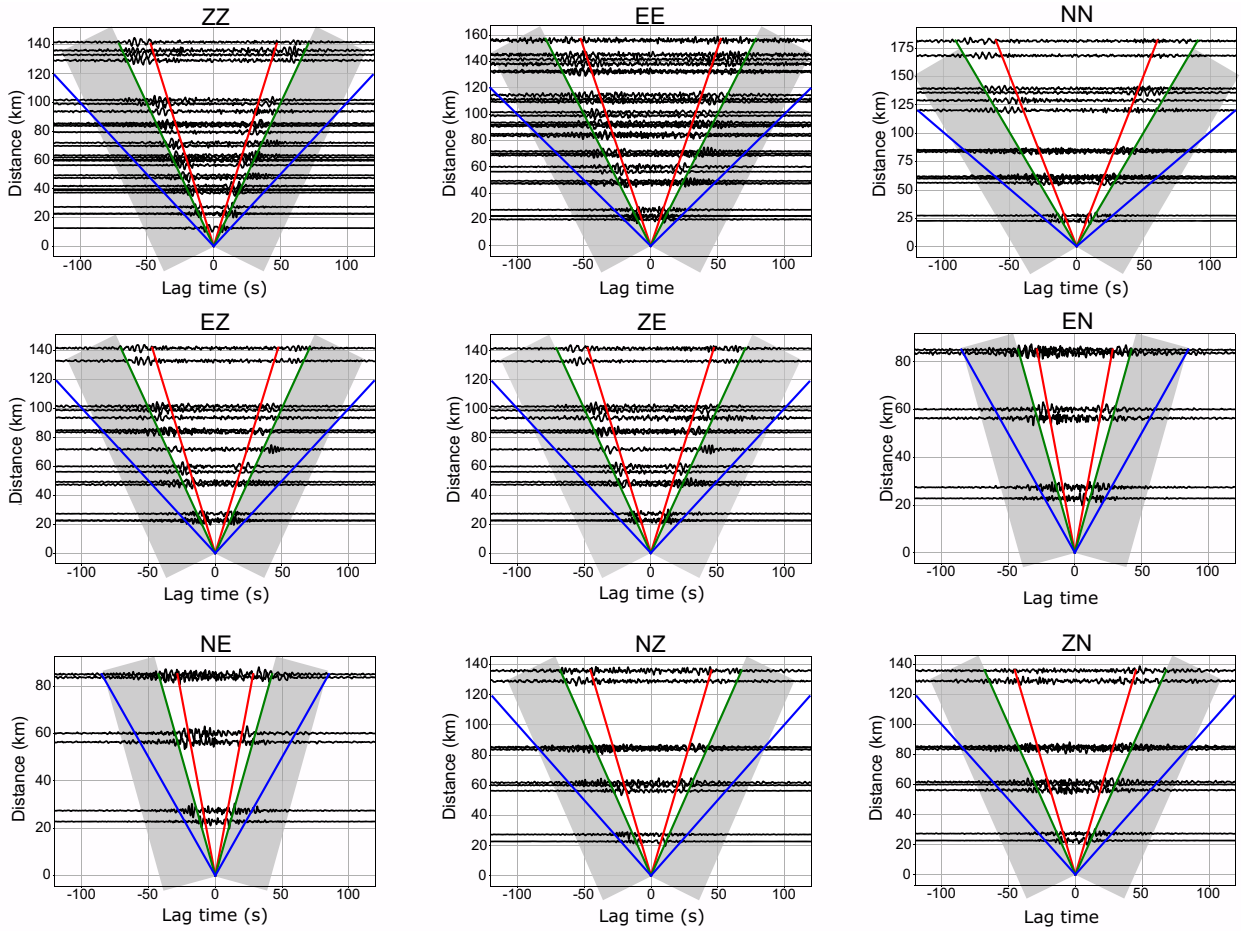

Figure 3. Plots of reference cross-correlation functions against interstation distance for all nine component pairs. Coda windows (lasting 40 s, starting at the velocity moveout of 2.0 km s^{-1}) are shown by transparent grey boxes. Velocity moveouts are shown by coloured lines: red = 3.0 km s^{-1}, green = 2.0 km s^{-1} and blue = 1.0 km s^{-1}. Radial and transverse components were not used.

3.4 Velocity variations

Relative velocity variations are computed by comparing the difference in arrival time between current stacks and the reference stack using the MWCS technique (Poupinet *et al.* 1984; Frechet *et al.* 1989; Clarke *et al.* 2011). Specifically, the delay time (δt) is measured in the frequency domain within a series of moving windows. We choose a window length of 20 s, shifting the window by 4 s between each measurement. The final velocity change is then computed from the slope of the delay times ($\delta t/t$), following:

$$\frac{\delta t}{t} = -\frac{\delta v}{v} \tag{1}$$

where $\delta v/v$ is the relative velocity variation, under the assumption of a homogeneously distributed change (Ratdomopurbo & Poupinet 1995; Lecocq *et al.* 2014). Certain quality control criteria are used to define which delay time measurements are used in the linear regression. These are the minimum coherence between the current and reference stack within each moving window (set to 0.8), the maximum delay time (0.2 s), and the maximum error of this delay time (0.1 s). Further details can be found in the supplementary material.

4 RESULTS

Fig. 4 shows the results for the full 6-yr data set with only the ZZ component (red line) compared to averaging all of the component pairs (blue line). The averaged velocity from all components show the smoother result, but both reveal a similar value of velocity decrease following the Kaikōura earthquake. With all of the component pairs, a velocity decrease of 0.19±0.08 per cent was observed, whereas using just the vertical–vertical component-pair a decrease of 0.23±0.09 per cent is recorded (Fig. 4 and Table 1).

Besides the 2016 Kaikōura earthquake, there were four other large-magnitude ($M_w > 5.6$) earthquakes that occurred in the 6-yr period, two in 2013, and one each in 2015 and 2016. In 2013, there was the Cook Strait earthquake (M_w 6.5 on 2013 July 21—163 km away from the 2016 Kaikōura rupture) and the Lake Grassmere earthquake (M_w 6.6 on 2013 August 16—144 km away from Kaikōura). These earthquakes were located only 17 km and 26 d apart, and both were shallow at 15.6 and 7.5 km depths respectively (Fig. 1, earthquakes 1 and 2). Despite both of these earthquakes being large events, no significant velocity changes are observed (Fig. 4).

A large earthquake occurred in April 2015 with a magnitude of M_w 6.2 and a depth of 52 km. Another earthquake, approximately 2 km away from the April 2015 earthquake, occurred in February 2016 with a magnitude of M_w 5.7 and a depth of 48 km (both are

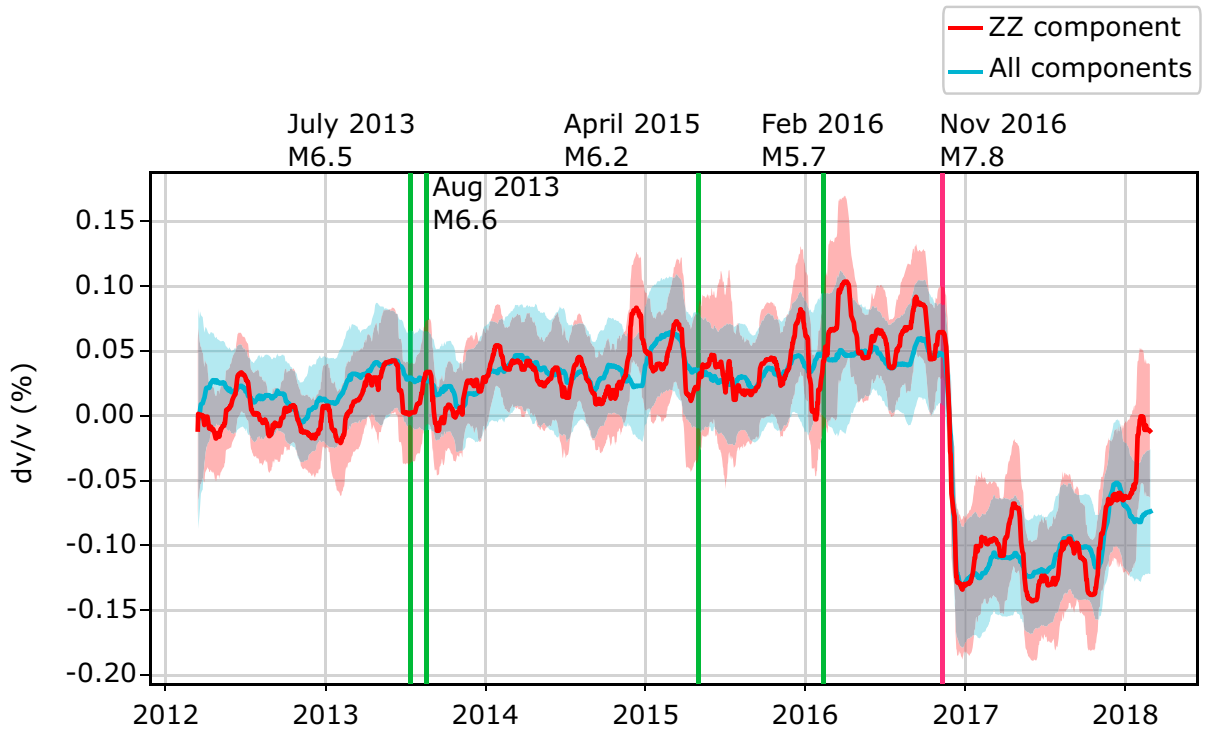

Figure 4. Velocity changes for only the ZZ component and for the average of all of the component pairs using the 6-yr data set, smoothed with a median 30-d moving average window (rolling). The solid lines are the averages and the light background colours are the matching standard errors. The 2016 Kaikōura earthquake is shown by the pink line with all other large-magnitude events ($M_w > 5.6$) in this time period shown in green.

shown in Fig. 1, earthquakes 3 and 4). Velocity changes are not observed immediately after these two events (Fig. 4). The stations closest to these earthquakes were not recording during this period of time and the two earthquakes are both deep (52 and 48 km). Prior to both earthquakes, velocity decreases are observed on the vertical–vertical component. As only a minor decrease is observed when using all of the component pairs, it is likely this is a consequence of using only a few stations and we assume it to be a spurious fluctuation.

Across the Kaikōura region the velocity decrease following the 2016 earthquake was observed on many station pairs with different interstation distances and varying distances from the Kaikōura earthquake and ruptured faults (Fig. 1). This includes station pairs at large distances from the epicentre and ruptured faults, for example SJQ–WJM at more than 100 km distance (see Fig. 1). Multiple station pairs suffered from data quality issues throughout the time period, and were therefore not included in the final measurement. This is demonstrated when comparing the correlation coefficient recorded for SJQ–WJM in Supporting Information Fig. S5 versus an example of a discarded station pair in Supporting Information Fig. S6. Further details can be found in Kortink (2020).

Similarly, due to data drop-outs on individual components, varying station pairs are used for each of the nine component pairs. The velocity decrease on individual component pairs as a result of the 2016 Kaikōura earthquake is shown in Fig. 5 and Table 1. This table also lists which stations are used for each component-pair. Following the earthquake, all of the component pairs experienced a decrease, with an average value of 0.19±0.08 per cent. This value differed between individual components, which could also be related to the use of different station pairs. Following the Kaikōura earthquake, we observe an average increase in the velocity over approximately 1.5 yr, with a vertical–vertical component-pair recording an increase of 0.15±0.11 per cent by the end of our data period. While a velocity increase cannot be confirmed across all component pairs when measurement uncertainty is taken into account, we note that mean value of $\delta v/v$ had increased in all cases (0.07 per cent increase on average). Thus, we feel this increasing velocity trend observed across component pairs is likely to reflect a recovery period following the co-seismic change.

5 DISCUSSION

A seismic velocity decrease of 0.19±0.08 per cent is measured from the average of all cross-component pairs following the 2016 Kaikōura earthquake. This is comparable to decreases observed in similar studies globally (e.g. see Section 1 and Supporting Information Table S5). Following the co-seismic velocity decrease, we measure an increase of 0.15±0.11 per cent over a 1.5-yr period for the vertical–vertical component (Fig. 5). An increase of 0.07 per cent is observed over the same period when all of the component pairs are averaged.

5.1 Depth resolution

We first consider the depth resolution under the assumption that the coda is dominated by surface waves. Because we focus on only the vertical–vertical results, we assume that scattered Rayleigh waves are most dominant. Therefore we analyse the depth resolution using Rayleigh wave group-velocity sensitivity kernels computed using codes by Herrmann (2013; Fig. 6). We used an average regional velocity model from Eberhart-Phillips & Fry (2018). The kernels were computed for 1–10 s (0.1–1 Hz), encompassing the frequency range of cross-correlation functions used in the

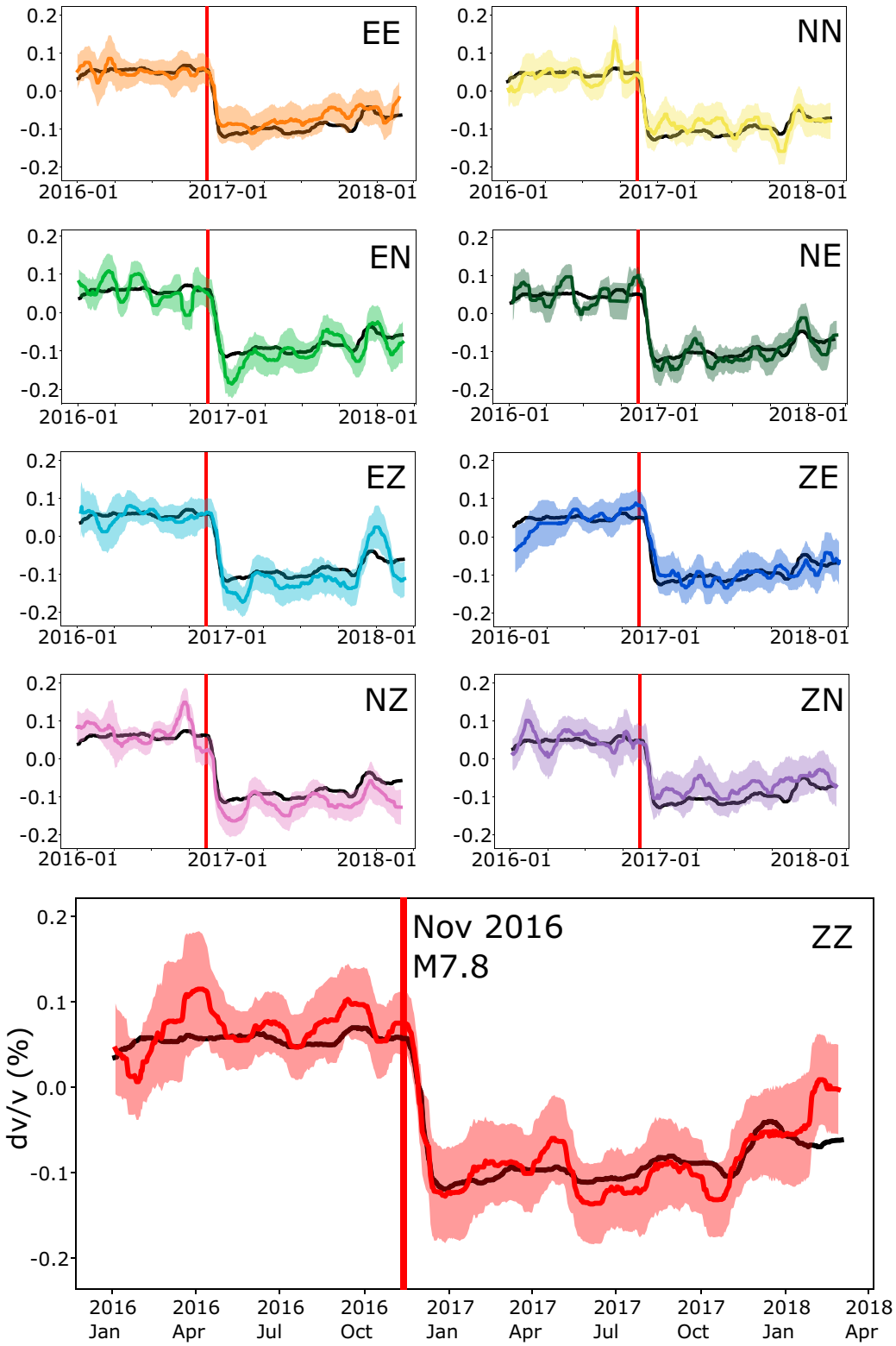

Figure 5. Velocity changes for nine component pairs from 2016 to 2018, smoothed with a median 30-d moving average window (rolling). In all plots, the black line plots the average of all of the component pairs, the solid coloured lines show the average for each component pair with the light background colours showing the standard error. The 2016 Kaikōura earthquake is shown by the red vertical line.

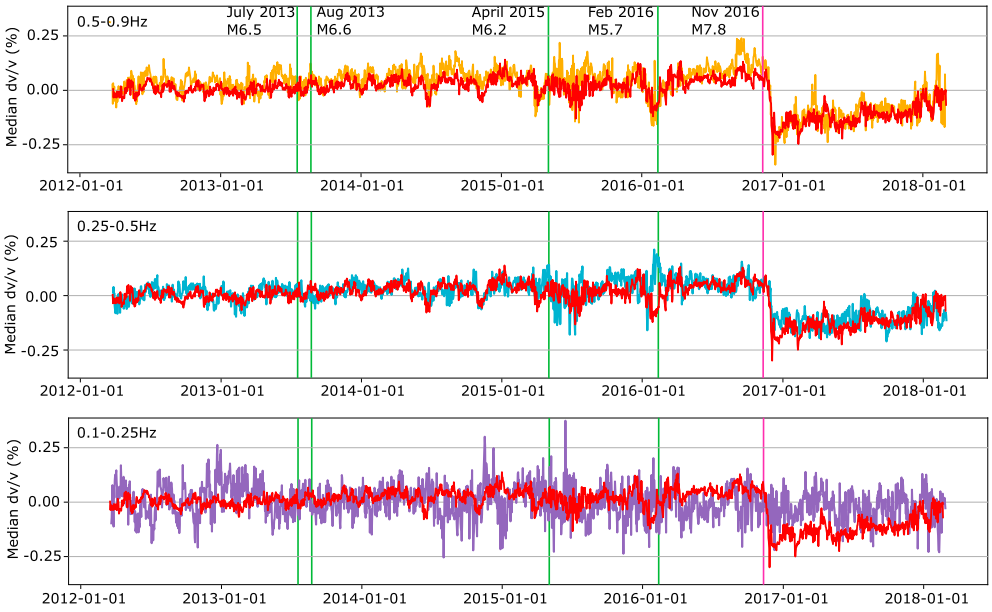

(a) Seismic Velocity Variation

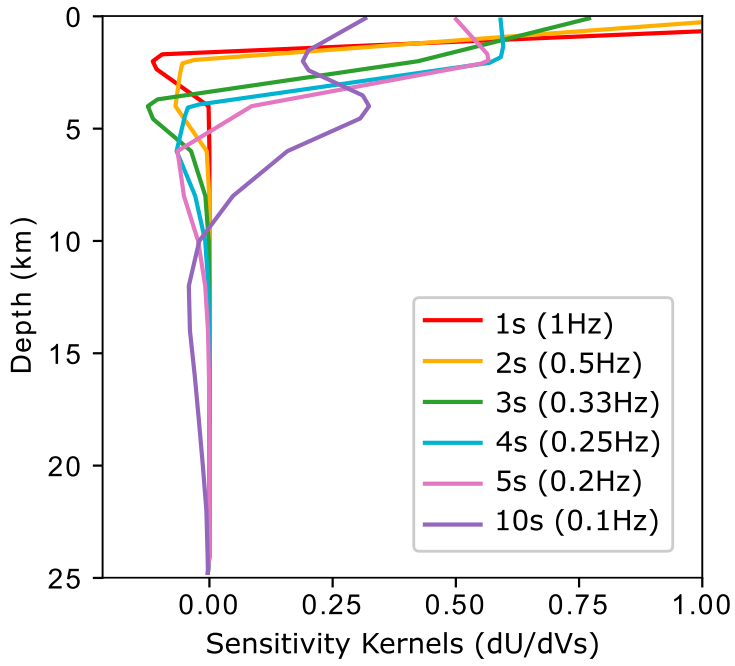

(b) Depth Sensitivity Kernels

Figure 6. Depth analysis. (a) Seismic velocity variations for the unsmoothed 30-d moving stacks vertical–vertical component pair in the period band 0.1–0.9 Hz (result in red in all plots) and three sub-bands of 0.1–0.25 Hz (purple line), 0.25–0.5 Hz (blue line) and 0.5–0.9 Hz (orange line), respectively, all unsmoothed. Nine stations were used: CVR, IKR, JSP, KVR, MLF, SJQ, SRB, SVR and WJM. The green vertical lines represent large-magnitude earthquakes ($M_w > 5.6$) with the pink line showing the 2016 Kaikōura earthquake. (b) Depth sensitivity kernels for the Kaikōura region. Derivatives of the fundamental-mode Rayleigh wave group velocity with respect to the shear wave velocity at periods corresponding to the minimum and maximum periods of the data set used in this study are presented. The derivatives are based on the average regional velocity model (Eberhart-Phillips & Fry 2018).

velocity change computation. Additionally, we show the velocity changes computed using narrower bands of 0.1–0.25 Hz (4–10 s), 0.25–0.5 Hz (2–4 s) and 0.5–0.9 Hz (Fig. 6a). Velocity decreases become steadily larger for frequencies higher than 0.25 Hz, with the largest decreases of up to 0.35 per cent occurring within the 0.5–0.9 Hz band. The 0.25–0.5 Hz results show a velocity decrease of 0.2 per cent, less than both 0.5–0.9 Hz and 0.1–0.9 Hz, our original frequency band. Lower frequencies of 0.1–0.25 Hz do not show a decrease in velocity following the 2016 Kaikōura earthquake.

From the fundamental mode Rayleigh wave sensitivity kernels, we see that the surface waves in the analysed frequency range (1–10 s) have little sensitivity below 5 km depth. The sensitivity kernels for the highest recorded velocity decreases of 0.35 per cent (frequency band 0.5–0.9 Hz) are in the uppermost 2 km (Fig. 6b). These observations are comparable with velocity changes from other large earthquakes. In California, following the 2003 San Simeon and the 2004 Parkfield earthquakes, Wu *et al.* (2016) showed that the velocity decreases were greatest for frequencies between 1–1.5 Hz. Nimiya *et al.* (2017) demonstrated similar results after the 2016 Kumamoto earthquake, where they found the largest change for frequencies greater than 1 Hz. The sensitivity of velocity change measurements has been shown to rapidly decay with depth (Obermann *et al.* 2013). It is possible then that the absence of an observable velocity change at lower frequencies reflects a loss of measurement sensitivity rather than an absence of a velocity perturbation.

A further complication in locating the depth of velocity changes relates to the contribution of body waves in the coda (Obermann *et al.* 2013, 2016; Yuan *et al.* 2021). In this case, a frequency dependent analysis of depth sensitivity may not be sufficient for determining the depth of velocity changes. One solution proposed by Obermann *et al.* (2013) is to analyse the lag time dependence on measurements of velocity change, with it suggested that $\delta v/v$ decreases will be greater at short lag times for shallow perturbations, and greater at long lag times for deeper perturbations. This follows the suggestion that later parts of the cross-correlation function have a stronger contribution from body-waves with greater depth sensitivity (Obermann *et al.* 2013, 2016). We apply this idea to station pair IKR–MLF, which recorded the largest velocity decrease and has data of sufficient quality to measure $\delta v/v$ at later lag times (Supporting Information Fig. S8). We observe a systematic change in $\delta v/v$ as the lag time window is shifted to later parts of the cross-correlation function, with the largest decreases recorded using earlier lag times and smallest decreases using later lag times (Supporting Information Fig. S8). This supports the argument that the velocity changes we observe are occurring at a shallow depth. Determining the relative contribution of body and surface waves in a natural environment remains challenging, however. Yuan *et al.* (2021) recently show that, while body waves may contribute equally in the mid-coda, scattered surface waves dominate once again in the late coda. Despite these complications, we observe no evidence in the analysis of frequency-dependent and lapse-time dependent velocity changes to support an argument of a deeper source and, therefore, prefer the interpretation of a shallow source of velocity change resulting from the Kaikōura earthquake.

5.2 Mechanisms

Several possible mechanisms for velocity changes following earthquakes have been proposed, as summarized by Xu & Song (2009) and Wegler *et al.* (2009). These are as follows: (1) static stress-induced changes of fault zone properties at seismogenic depth, (2) damage of shallow crust from strong-ground shaking, (3) damage of the crust from fault zone rupture and (4) rapid changes in groundwater near the surface or fluid activities in the shallow crust.

Static stress-induced velocity changes can be caused by the preferential opening or closing of pre-existing cracks due to the change in stress (Rubinstein & Beroza 2004). Assuming pre-existing cracks are isotropically distributed, velocities should increase in regions of decreased mean stress (increased compression) and decrease in regions of increased mean stress (increased dilation). This is because the stress would preferentially close cracks in the case of compression and open cracks in the case of dilation (Nur 1971; Dodge & Beroza 1997; Rubinstein & Beroza 2004). We observe little evidence that any regions experienced a velocity increase as a result of the Kaikōura earthquake, with only velocity decreases observed. This observation is consistent with other studies of seismic velocity changes after large earthquakes, which similarly note the lack of velocity increases as a means to exclude static stress-induced changes as the primary cause (e.g. Rubinstein & Beroza 2004; Wegler *et al.* 2009). We therefore consider it unlikely that the velocity decreases following the 2016 Kaikōura earthquake are primarily related to static stress-induced changes.

Near-surface damage as a result of strong ground motions has regularly been linked to velocity reductions following large earthquakes (e.g. Schaff & Beroza 2004; Sawazaki *et al.* 2009; Nakata & Snieder 2011; Chaves & Schwartz 2016; Nimiya *et al.* 2017; Viens *et al.* 2018; Bonilla *et al.* 2019). Such strong motions can produce nonlinear effects in shallow soils in response to large dynamic strains (Beresnev & Wen 1996). Characteristic of this mechanism is a widespread velocity decrease, with a magnitude of change correlated with the level of ground shaking. We explore this mechanism further by investigating the relationship between peak ground velocities (PGV) and seismic velocity changes recorded using different station pairs (Fig. 7). For measurements of PGV, we use simulated values produced by Bradley *et al.* (2017). These were shown to be in good agreement with amplitudes recorded using GeoNet stations (Bradley *et al.* 2017), and allow us to assign a value of PGV at each station. We could not calculate PGV directly from our stations because many of them were affected by amplitude clipping during the Kaikōura earthquake. For measurements of velocity change associated with the earthquake, we measure the average $\delta v/v$ within two 10-d windows (Supporting Information Fig. S7). These are used to record $\delta v/v$ both before and after the earthquake, with the position of the second window chosen to ensure the 30-d stacks consist only of cross-correlation functions computed using post-earthquake seismic data. For multiple pairs, issues with measurement quality immediately after the earthquake meant the post-earthquake $\delta v/v$ measurement was taken at a later time (Supporting Information Table S6). Such measurements then represent minimum estimates of the co-seismic velocity change.

For direct comparison with PGV values we evaluate the $\delta v/v$ change at each station by least-squares inversion, following the approach of Hobiger *et al.* (2012). Specifically, the velocity change observed by a pair of stations is considered to be the average of the velocity change that occurs at each station, i.e.

$$\Delta_{\mathrm{obs},i} = (\Delta_{\mathrm{station},i_1} + \Delta_{\mathrm{station},i_2})/2$$

where $\Delta_{obs,\,i}$ is the observed velocity change for station pair i, and $\Delta_{\mathrm{station},i_1}$ and $\Delta_{\mathrm{station},i_2}$ are the changes that actually occurred at stations i_1 and i_2 respectively. The inversion problem is then defined as

$$\vec{\Delta}_{\mathrm{obs}} = \mathbf{M} \cdot \vec{\Delta}_{\mathrm{station}}$$

where $\vec{\Delta}_{\mathrm{obs}}$ is the vector of observed velocity changes, $\vec{\Delta}_{\mathrm{station}}$ the vector of velocity changes at different stations to solve for, and the matrix $\mathbf{M}$ indicating which single stations contribute to each observation. This formulation of the problem represents a greatly simplified version of sensitivity kernels calculated for wave scattering media, where it is shown that changes between two sensors mostly originate in close proximity to both stations (Pacheco & Snieder 2005, 2006; Hobiger *et al.* 2012). It is highly unlikely in reality that the observed velocity is the exact average between two stations, especially

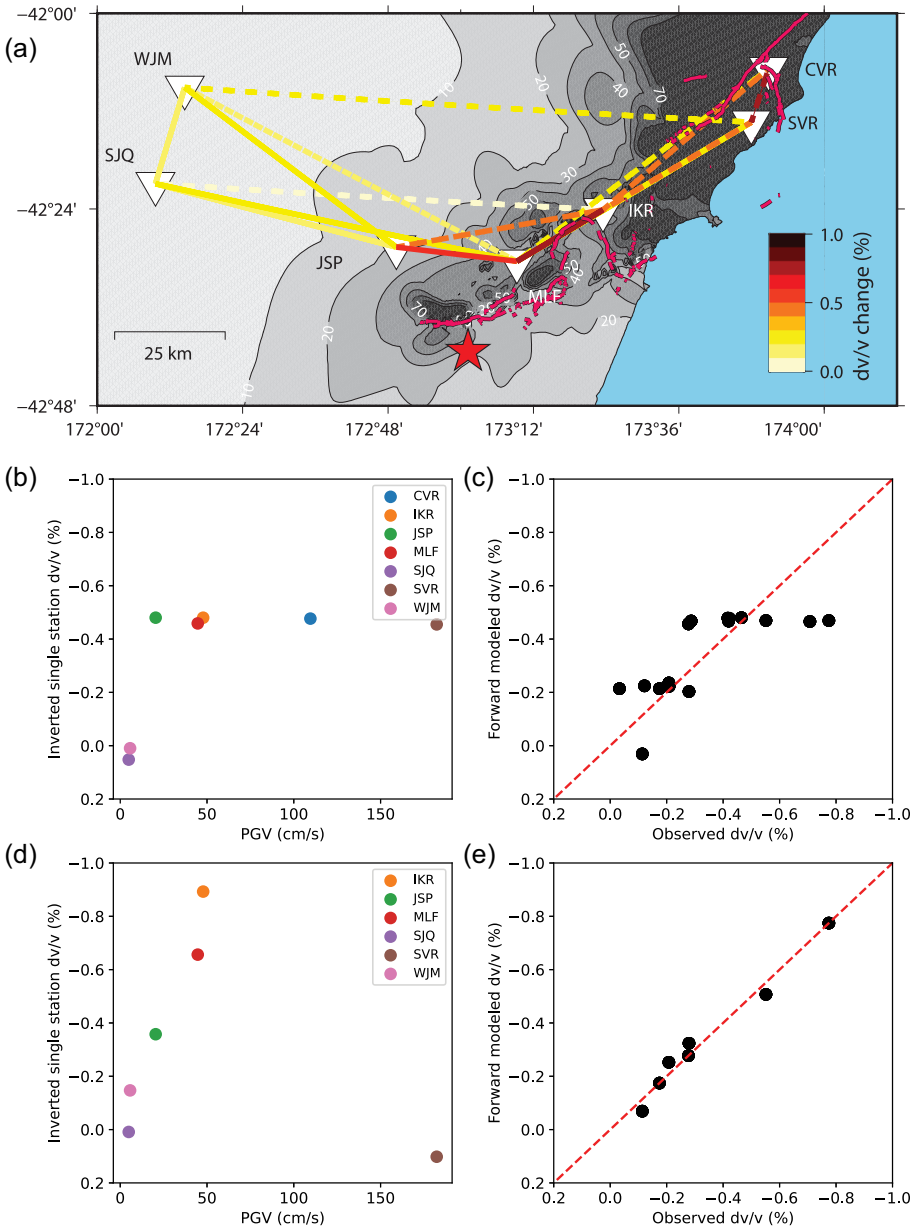

Figure 7. Comparison between velocity changes recorded after the 2016 Kaikōura earthquake and simulated PGV values from Bradley *et al.* (2017). (a) Co-seismic velocity decreases overlaying simulated PGV. Dashed lines indicate a minimum estimate of $\delta v/v$ due to the need to use a later measurement window (Supporting Information Table S6). Pink fault lines are also displayed as in Fig. 1. (b) Plot of PGV against estimated values of $\delta v/v$ at individual single stations through inversion when using all station pairs. (c) Plot of observed $\delta v/v$ from station pairs and forward modelled $\delta v/v$ using single-station values in (b). (d and e) As with (c) and (d), but with only station pairs that allowed measurements to be made immediately following the earthquake.

if velocity changes are not homogeneous. However, for our purposes this simple approach can still provide some insight into which locations likely experienced larger $\delta v/v$ changes, and allows for easier comparison with PGV estimates. Finally, we assess the inverted values of $\delta v/v$ at individual stations by computing the forward model. If the forward modelled station pair $\delta v/v$ approximately resemble those observed in this study, we can be more confident in the inversion results.

Results are shown for both the inversion using all station pairs (Figs 7b and c) and for the inversion using only station pairs where a measurement was possible immediately after the earthquake (Figs 7d and e). When all station pairs are used for the inversion, we do not observe a good fit between the observed and forward modelled $\delta v/v$ (Fig. 7c). In particular, the variation in $\delta v/v$ measured across the different station pairs is not well-recovered. We also note that a velocity increase is resolved at both SJQ and WJM stations individually (Fig. 7b), despite a velocity decrease being observed for the pair SJQ-WJM. We suspect the usage of station pairs where the velocity change could not be measured immediately after the earthquake has contributed to the poor fit. In contrast, the inversion using only station pairs where a measurement was available immediately following the earthquake demonstrates a better fit between observed and forward modelled $\delta v/v$ (Fig. 7e). Focusing on the relationship between PGV and inverted estimates of $\delta v/v$ at each station, we observe an increasing velocity change as PGV increases up to ∼50 cm s^{-1} (Fig. 7d), consistent with a model of ground-shaking induced

velocity changes. At SVR station, however, the resolved $\delta v/v$ shows a small velocity increase following the earthquake despite having a simulated PGV of nearly 200 cm s^{-1}. It is possible that this relates to the low number of station pairs used in the inversion (only one pair that includes SVR station, MLF-SVR). However, it could also indicate that strong ground shaking is not entirely responsible for the observed velocity changes at this site, where we note that the inclusion of additional pairs that use SVR has minimal influence on the magnitude of resolved $\delta v/v$ at this station (Supporting Information Fig. S9), although it reverses its sign to show a slight velocity decrease. The location of this station is particularly interesting; it sits on the hanging wall of the Papatea fault, which experienced significant uplift as a consequence of the earthquake (∼9.5m max, Langridge *et al.* (2018)). Recent work analysing aftershock locations has suggested the Papatea fault may have acted in a similar style to a restraining bend, where it sits at the corner of dominantly thrust motion offshore and sinistral-normal oblique motion onshore (Chamberlain *et al.* 2021). In this scenario, we may expect that compression within the hanging wall of the Papatea fault (consistent with a velocity increase) could be counter-acting the expected velocity decrease associated with strong-ground shaking, therefore producing a lower magnitude of change. Improved spatial analysis of the $\delta v/v$ is necessary, however, to shed further light on this hypothesis.

A further difficulty in assessing the mechanism of observed velocity changes associated with the Kaikōura earthquake relates to the extensive region of fault ruptures, where as many as 21 faults ruptured during the earthquake sequence (Stirling *et al.* 2017; Klinger *et al.* 2018). Damage of the crust from rupture of the fault zone would be expected to produce an initial velocity decrease in the vicinity of ruptured faults, followed by a velocity increase as crack healing occurs. Characteristic of this would be that velocity changes should be large for station-paths that cross ruptured faults and small for paths that don't (Rubinstein & Beroza 2004). However, with many of our stations lying in close proximity to ruptured faults, it is not straightforward to deduce whether a relationship between PGV and $\delta v/v$ reflects strong-ground motion induced damage or fault-zone damage as the primary cause of velocity changes, given that sites in the vicinity of rupture zones tend to experience stronger shaking. We note that the largest observed velocity change was recorded by the station pair IKR–MLF, which has a direct path that crosses mapped surface ruptures (Fig. 7). Thus we cannot rule out fault zone damage as a contributing factor in our velocity change measurements. However, observations of a velocity decrease at more distant stations (e.g. SJQ–WJM) suggests another mechanism, such as strong-ground shaking, is needed to explain our results.

Finally, groundwater responses and other fluid movements can also cause changes in seismic velocities (Sens-Schönfelder & Wegler 2006; Meier *et al.* 2010; Lecocq *et al.* 2017; Clements & Denolle 2018; He & Singh 2019). Following the Kaikōura earthquake, Weaver *et al.* (2019) observed both positive and negative water level changes at distances between 4 and 850 km from the 2016 Kaikōura earthquake epicentre. The time taken for water levels to re-equilibrate at new post-earthquake levels generally ranged from 10 min to 2 hr, with a median time of 65 min and the longest time of 100 + days (at Cromwell Gorge) (Weaver *et al.* 2019). Sites experiencing lower levels of ground shaking produced approximately equal numbers of water level increases and decreases, whereas sites experiencing a PGA above approximately 2 m s^{-2} and PGV above 0.3 m s^{-1} (or 30 cm s^{-1}) produced predominantly water level increases (Weaver *et al.* 2019). An increase in the water level is consistent with a velocity decrease (Clements & Denolle 2018), and therefore could be a contributing factor. It is not straightforward however to separate groundwater induced changes from damage in the shallow crust as the dominant mechanism without further comparison of these two data sets, with increased spatial resolution of velocity changes. In both cases, though, strong ground shaking can be considered a probable cause, especially at seismic stations that are most distant from the fault ruptures.

5.3 Pre-Kaikōura events

In the 6-yr data set it was also possible to determine if any other large-magnitude ($M_w > 5.6$) events caused changes in the seismic velocity. We considered the Cook Strait and Lake Grassmere earthquakes in 2013 (M_w 6.5 and M_w 6.6 respectively) and two additional earthquakes (M_w 6.2 and M_w 5.7) in 2015 and 2016 respectively that, while smaller in magnitude, were closer to our network. None of these showed a velocity decrease that could be easily distinguished from background fluctuation of velocity changes (Fig. 4).

Possible explanations for the lack of observed velocity changes associated with these earthquakes are their locations relative to the network and lower magnitudes. Both the Cook Strait and Lake Grassmere earthquakes occurred just outside the network (Fig. 1). Furthermore, the five closest stations (CCB, CVR, IKR, KVR and SVR) were either unavailable during this period, or were not usable due to large gaps in the data (Supporting Information Fig. S1). Finally, the averaging time window (30 d) is larger than the time separation of the events (26 d), so the effect of both earthquakes may be muted. For comparison with the Kaikōura earthquake, we compute the PGV for two strong motion sensors located within our network (Supporting Information Figs S10 and S11). One of these (MOLS) is in close proximity to the epicentres of the M_w 6.2 and M_w 5.7 earthquakes in 2015 and 2016 respectively, while the other (WTMC) is close to the epicentre of the Kaikōura earthquake. The PGV at these stations is far lower than those produced by the Kaikōura earthquake (Supporting Information Table S2). For the Cook Strait and Lake Grassmere earthquakes, the PGV recorded by both sensors is less than 2.5 cm s^{-1}, and less than 4 cm s^{-1} for the M_w 5.7 in 2016. A PGV of 17 cm s^{-1} was, however, recorded by one of the strong-motion sensors (MOLS) in response to the M_w 6.2 earthquake in 2015. However, this value likely reflects the close proximity of the earthquake to the sensor rather than representing significant shaking across the network. This is demonstrated by a PGV of 2.5 cm s^{-1} at the second sensor (WTMC) for the same event.

Of interest is that Civilini *et al.* (2020) found a velocity decrease of 0.06 per cent at Ngatamariki Geothermal Field following the Cook Strait and Lake Grassmere earthquakes, using stations located in the Taupō Volcanic Zone. This was despite these earthquakes occurring approximately 400 km away, far greater than the distance between these earthquakes and our network. Such changes at larger distances may reflect increased sensitivity to velocity changes within geothermal regions. Brenguier *et al.* (2014) found that following the 2011 M_w 9.0 Tohoku-Oki earthquake, the strongest co-seismic velocity reductions occurred under volcanic regions rather than in regions with the most intense ground shaking or co-seismic deformation. They suggest that regions with low effective pressure, such as volcanic or geothermal regions, are more susceptible to velocity changes and dynamic stress changes due to cracks opening and increasing the permeability and transfer of fluids (Brenguier *et al.* 2014).

6 CONCLUSION

We used the signals of cross-correlation functions generated from ambient noise to determine velocity changes in the Kaikōura region in order to examine changes before and after the M_w 7.8 2016 Kaikōura earthquake. The time period chosen for this study, 2012–2018, also included four other large-magnitude events in the region in 2013 and 2015–2016.

Following the 2016 Kaikōura earthquake, average velocity decreases of up to 0.19±0.08 per cent were observed down to about 5 km depth across all nine components of the Green's function tensor, with the largest velocity decreases in the uppermost 2.5 km. A velocity increase of about 0.07 per cent was observed in the 1.5 yr after the earthquake. We did not observe a velocity change following the 2013 Cook Strait earthquake sequence or the Lake Grassmere earthquake, while changes associated with other large earthquakes in 2015 and early 2016 were ambiguous. We infer that velocity reductions following the 2016 Kaikōura earthquake were at least partially caused by strong near-surface ground motions, followed by subsequent crack healing that increased the seismic velocity. It is also possible that fault-zone damage contributed to velocity decreases, where we note that many of the analysed stations are located in the vicinity of ruptured faults. Improved spatial resolution of velocity changes is necessary to assess the relative contribution of these two mechanisms.

ACKNOWLEDGEMENTS

This work was funded by New Zealand Earthquake Commission Biennial Grant program Project 18/755 and 20796, and the Frank Evison Research Scholarship in Geophysics, administered by Victoria University of Wellington. The short-period seismometers were deployed and serviced by Kyoto and Tohoku University. This study was supported by the Ministry of Education, Culture, Sports, Science and Technology (MEXT) of Japan, under its The Second Earthquake and Volcano Hazards Observation and Research Program (Earthquake and Volcano Hazard Reduction Research) (Grant Number: THK01). We acknowledge the New Zealand GeoNet project and its sponsors EQC, GNS Science, LINZ, NEMA and MBIE for providing data used in this study. The GeoNet Quake Search was valuable in providing earthquake information. Thoughtful comments and suggestions by Finnigan Illsley-Kemp, Susan Schwartz, Marine Denolle, Thomas Lecocq and an anonymous reviewer helped to greatly improve this paper. Thanks also go to Brendon Bradley for providing the PGV values from his paper (Bradley *et al.* 2017). We acknowledge the New Zealand GeoNet project and its sponsors EQC, GNS Science, LINZ, NEMA and MBIE for providing data used in this study.

DATA AVAILABILITY

The MSNoise codes used to calculate cross correlation functions are available on GitHub at https://github.com/ROBelgium/MSNoise.

Please contact authors Martha Savage or Tomomi Okada if you are interested in accessing the raw data from the temporary stations.

REFERENCES

Bensen, G.D., Ritzwoller, M.H., Barmin, M.P., Levshin, A.L., Lin, F., Moschetti, M.P., Shapiro, N.M. & Yang, Y., 2007. Processing seismic ambient noise data to obtain reliable broad-band surface wave dispersion measurements, *Geophys. J. Int.,* **169**(3), 1239–1260.

Beresnev, I.A. & Wen, K.-L., 1996. Nonlinear soil response—a reality?, *Bull. seism. Soc. Am.,* **86**(6), 1964–1978.

Bonilla, L.F., Guéguen, P. & Ben-Zion, Y., 2019. Monitoring coseismic temporal changes of shallow material during strong ground motion with interferometry and autocorrelation, *Bull. seism. Soc. Am.,* **109**(1), 187–198.

Bradley, B.A., Razafindrakoto, H. N.T. & Nazer, M., 2017. Strong ground motion observations of engineering interest from the 14 November 2016 M_w7.8 Kaikōura, New Zealand earthquake, *Bull. N.Z. Soc. Earthq. Eng.,* **50,** 85–93.

Brenguier, F., Campillo, M., Hadziioannou, C., Shapiro, N.M., Nadeau, R.M. & Larose, E., 2008. Postseismic relaxation along the San Andreas fault at Parkfield from continuous seismological observations, *Science,* **321**(5895), 1478–1481.

Brenguier, F., Campillo, M., Takeda, T., Aoki, Y., Shapiro, N.M., Briand, X., Emoto, K. & Miyake, H., 2014. Mapping pressurized volcanic fluids from induced crustal seismic velocity drops, *Science,* **345**(6192), 80–82.

Brenguier, F., Shapiro, N.M., Campillo, M., Nercessian, A. & Ferrazzini, V., 2007. 3-D surface wave tomography of the Piton de la Fournaise volcano using seismic noise correlations, *Geophys. Res. Lett.,* **34**(2), doi:10.1029/2006GL028586.

Chamberlain, C.J., Frank, W.B., Lanza, F., Townend, J. & Warren-Smith, E., 2021. Illuminating the pre-, co-, and post-seismic phases of the 2016 M7.8 Kaikōura earthquake with 10 years of seismicity, *J. geophys. Res.,* **126**(8), e2021JB022304.

Chaves, E.J. & Schwartz, S.Y., 2016. Monitoring transient changes within overpressured regions of subduction zones using ambient seismic noise, *Sci. Adv.,* **2**(1), e1501289.

Civilini, F., 2018. Determining seismic shear-velocity from ambient noise sources at regional and local scales, *PhD thesis*, Victoria University of Wellington.

Civilini, F., Savage, M.K. & Townend, J., 2020. Shear wave velocity changes induced by earthquakes and rainfall at the Rotokawa and Ngatamariki geothermal fields, Taupō Volcanic Zone, New Zealand, *Geophys. J. Int.,* **221**(1), 97–114.

Clark, K.J. *et al.*, 2017. Highly variable coastal deformation in the 2016 M_w7.8 Kaikōura earthquake reflects rupture complexity along a transpressional plate boundary, *Earth planet. Sci. Lett.,* **474,** 334–344.

Clarke, D., Zaccarelli, L., Shapiro, N.M. & Brenguier, F., 2011. Assessment of resolution and accuracy of the moving window cross spectral technique for monitoring crustal temporal variations using ambient seismic noise, *Geophys. J. Int.,* **186**(2), 867–882.

Clements, T. & Denolle, M.A., 2018. Tracking groundwater levels using the ambient seismic field, *Geophys. Res. Lett.,* **45**(13), 6459–6465.

Dodge, D.A. & Beroza, G.C., 1997. Source array analysis of coda waves near the 1989 Loma Prieta, California, mainshock: implications for the mechanism of coseismic velocity changes, *J. geophys. Res.,* **102**(B11), 24 437–24 458.

Eberhart-Phillips, D. & Fry, B., 2018. Joint local earthquake and teleseismic inversion for 3-D velocity and Q in New Zealand, *Phys. Earth planet. Inter.,* **283,** 48–66.

Frechet, J., Martel, L., Nikolla, L. & Poupinet, G., 1989. Application of the cross-spectral moving-window technique (CSMWT) to the seismic monitoring of forced fluid migration in a rock mass, *Int. J. Rock Mech. Min. Sci. Geomech. Abstr.,* **26,** 221–233.

Froment, B., Campillo, M., Chen, J.H. & Liu, Q.Y., 2013. Deformation at depth associated with the 12 May 2008 M_w 7.9 Wenchuan earthquake from seismic ambient noise monitoring, *Geophys. Res. Lett.,* **40**(1), 78–82.

Hadziioannou, C., Larose, E., Baig, A., Roux, P. & Campillo, M., 2011. Improving temporal resolution in ambient noise monitoring of seismic wave speed, *J. geophys. Res.,* **116**(B7), doi:10.1029/2011JB008200.

Hamling, I.J. *et al.*, 2017. Complex multifault rupture during the 2016 M_w 7.8 Kaikōura earthquake, New Zealand, *Science,* **356**(6334), eaam7194.

He, A. & Singh, R.P., 2019. Groundwater level response to the Wenchuan earthquake of May 2008, *Geomatics, Nat. Hazards Risk,* **10**(1), 336–352.

Heckels, R. E.G., Savage, M.K. & Townend, J., 2018. Post-seismic velocity changes following the 2010 M_w 7.1 Darfield earthquake, New Zealand,

revealed by ambient seismic field analysis, *Geophys. J. Int.,* **213**(2), 931–939.

Heckels, R., 2017. Using ambient seismic noise to study temporal and spatial surface wave velocity structures and ambient noise field characteristics of central South Island, New Zealand, *PhD thesis*, Victoria University of Wellington.

Herrmann, R.B., 2013. Computer programs in seismology: an evolving tool for instruction and research, *Seismol. Res. Lett.,* **84**(6), 1081–1088.

Hobiger, M., Wegler, U., Shiomi, K. & Nakahara, H., 2012. Coseismic and postseismic elastic wave velocity variations caused by the 2008 Iwate-Miyagi Nairiku earthquake, Japan, *J. geophys. Res.,* **117**(B9), doi:10.1029/2012JB009402.

Ikeda, T. & Tsuji, T., 2018. Temporal change in seismic velocity associated with an offshore M_w 5.9 Off-Mie earthquake in the Nankai subduction zone from ambient noise cross-correlation, *Prog. Earth planet. Sci.,* **5**(1), 1–12.

Klinger, Y. *et al.*, 2018. Earthquake damage patterns resolve complex rupture processes, *Geophys. Res. Lett.,* **45**(19), 10 279–10 287.

Kortink, M., 2020. Effect of the Kaikōura earthquake on velocity changes in and around the ruptured region: a noise cross correlation approach, *MSc thesis*, Victoria University of Wellington.

Langridge, R.M. *et al.*, 2016. The New Zealand active faults database, *N.Z. J. Geol. Geophys.,* **59**(1), 86–96.

Langridge, R.M. *et al.*, 2018. Coseismic rupture and preliminary slip estimates for the Papatea fault and its role in the 2016 M w 7.8 Kaikōura, New Zealand, Earthquake, *Bull. seism. Soc. Am.,* **108**(3B), 1596–1622.

Larose, E., Roux, P. & Campillo, M., 2007. Reconstruction of Rayleigh-Lamb dispersion spectrum based on noise obtained from an air-jet forcing, *J. acoust. Soc. Am.,* **122**(6), 3437–3444.

Lecocq, T., Caudron, C. & Brenguier, F., 2014. MSNoise, a python package for monitoring seismic velocity changes using ambient seismic noise, *Seismol. Res. Lett.,* **85**(3), 715–726.

Lecocq, T., Longuevergne, L., Pedersen, H.A., Brenguier, F. & Stammler, K., 2017. Monitoring ground water storage at mesoscale using seismic noise: 30 years of continuous observation and thermo-elastic and hydrological modeling, *Sci. Rep.,* **7**(1), 1–16.

Litchfield, N. *et al.*, 2017. 14th November 2016 M7. 8 Kaikōura earthquake. Summary surface fault rupture traces and displacement measurements, *GNS Sci.,* **10,** G21422RC21427C.

Meier, U., Shapiro, N.M. & Brenguier, F., 2010. Detecting seasonal variations in seismic velocities within Los Angeles basin from correlations of ambient seismic noise, *Geophys. J. Int.,* **181**(2), 985–996.

Minato, S., Tsuji, T., Ohmi, S. & Matsuoka, T., 2012. Monitoring seismic velocity change caused by the 2011 Tohoku-oki earthquake using ambient noise records, *Geophys. Res. Lett.,* **39**(9), doi:10.1029/2012GL051405.

Mordret, A., Landès, M., Shapiro, N.M., Singh, S.C., Roux, P. & Barkved, O.I., 2013. Near-surface study at the Valhall oil field from ambient noise surface wave tomography, *Geophys. J. Int.,* **193**(3), 1627–1643.

Nakata, N. & Snieder, R., 2011. Near-surface weakening in Japan after the 201 Tohoku-Oki earthquake, *Geophys. Res. Lett.,* **38**(17), doi:10.1029/2011GL048800.

Nimiya, H., Ikeda, T. & Tsuji, T., 2017. Spatial and temporal seismic velocity changes on Kyushu Island during the 2016 Kumamoto earthquake, *Sci. Adv.,* **3**(11), e1700813.

Nur, A., 1971. Effects of stress on velocity anisotropy in rocks with cracks, *J. geophys. Res.,* **76**(8), 2022–2034.

Obermann, A. & Hillers, G., 2019. Seismic time-lapse interferometry across scales, in *Advances in Geophysics,* Vol. 60, pp. 65–143, ed. Schmelzbach, C., Elsevier.

Obermann, A., Planes, T., Hadziioannou, C. & Campillo, M., 2016. Lapse-time-dependent coda-wave depth sensitivity to local velocity perturbations in 3-D heterogeneous elastic media, *Geophys. J. Int.,* **207**(1), 59–66.

Obermann, A., Planes, T., Larose, E., Sens-Schönfelder, C. & Campillo, M., 2013. Depth sensitivity of seismic coda waves to velocity perturbations in an elastic heterogeneous medium, *Geophys. J. Int.,* **194**(1), 372–382.

Okada, T. *et al.*, 2019. Comparative tomography of reverse-slip and strike-slip seismotectonic provinces in the northern South Island, New Zealand, *Tectonophysics,* **765,** 172–186.

Pacheco, C. & Snieder, R., 2005. Time-lapse travel time change of multiply scattered acoustic waves, *J. acoust. Soc. Am.,* **118**(3), 1300–1310.

Pacheco, C. & Snieder, R., 2006. Time-lapse traveltime change of singly scattered acoustic waves, *Geophys. J. Int.,* **165**(2), 485–500.

Poupinet, G., Ellsworth, W.L. & Frechet, J., 1984. Monitoring velocity variations in the crust using earthquake doublets: an application to the Calaveras Fault, California, *J. geophys. Res.,* **89**(B7), 5719–5731.

Ratdomopurbo, A. & Poupinet, G., 1995. Monitoring a temporal change of seismic velocity in a volcano: application to the 1992 eruption of Mt. Merapi (Indonesia), *Geophys. Res. Lett.,* **22**(7), 775–778.

Rubinstein, J.L. & Beroza, G.C., 2004. Evidence for widespread nonlinear strong ground motion in the M_w 6.9 Loma Prieta earthquake, *Bull. seism. Soc. Am.,* **94**(5), 1595–1608.

Savage, M.K., Lin, F. & Townend, J., 2013. Ambient noise cross-correlation observations of fundamental and higher-mode Rayleigh wave propagation governed by basement resonance, *Geophys. Res. Lett.,* **40**(14), 3556–3561.

Sawazaki, K., Sato, H., Nakahara, H. & Nishimura, T., 2009. Time-lapse changes of seismic velocity in the shallow ground caused by strong ground motion shock of the 2000 Western-Tottori earthquake, Japan, as revealed from coda deconvolution analysis, *Bull. seism. Soc. Am.,* **99**(1), 352–366.

Schaff, D.P. & Beroza, G.C., 2004. Coseismic and postseismic velocity changes measured by repeating earthquakes, *J. geophys. Res.,* **109**(B10), doi:10.1029/2006GL027797.

Sens-Schönfelder, C. & Wegler, U., 2006. Passive image interferometry and seasonal variations of seismic velocities at Merapi Volcano, Indonesia, *Geophys. Res. Lett.,* **33**(21), doi:10.1029/2006GL027797.

Shapiro, N.M. & Campillo, M., 2004. Emergence of broadband Rayleigh waves from correlations of the ambient seismic noise, *Geophys. Res. Lett.,* **31**(7), doi:10.1029/2004GL019491.

Snieder, R., Grêt, A., Douma, H. & Scales, J., 2002. Coda wave interferometry for estimating nonlinear behavior in seismic velocity, *Science,* **295**(5563), 2253–2255.

Stirling, M.W. *et al.*, 2017. The Mw 7.8 2016 Kaikōura earthquake: Surface fault rupture and seismic hazard context, *Bull. N.Z. Soc. Earthq. Eng.,* **50**(2), 73–84.

Taira, T., Brenguier, F. & Kong, Q., 2015. Ambient noise-based monitoring of seismic velocity changes associated with the 2014 Mw 6.0 South Napa earthquake, *Geophys. Res. Lett.,* **42**(17), 6997–7004.

Viens, L., Denolle, M.A., Hirata, N. & Nakagawa, S., 2018. Complex near-surface rheology inferred from the response of greater Tokyo to strong ground motions, *J. geophys. Res.,* **123**(7), 5710–5729.

Weaver, K.C., Cox, S.C., Townend, J., Rutter, H., Hamling, I.J. & Holden, C., 2019. Seismological and hydrogeological controls on New Zealand-wide groundwater level changes induced by the 2016 M_w 7.8 Kaikōura earthquake, *Geofluids,* **2019,** doi:10.1155/2019/9809458.

Wegler, U., Nakahara, H., Sens-Schönfelder, C., Korn, M. & Shiomi, K., 2009. Sudden drop of seismic velocity after the 2004 Mw 6.6 mid-Niigata earthquake, Japan, observed with Passive Image Interferometry, *J. geophys. Res.,* **114**(B6), doi:10.1029/2008JB005869.

Wegler, U. & Sens-Schönfelder, C., 2007. Fault zone monitoring with passive image interferometry, *Geophys. J. Int.,* **168**(3), 1029–1033.

Wu, C., Delorey, A., Brenguier, F., Hadziioannou, C., Daub, E.G. & Johnson, P., 2016. Constraining depth range of S wave velocity decrease after large earthquakes near Parkfield, California, *Geophys. Res. Lett.,* **43**(12), 6129–6136.

Xu, Z.J. & Song, X., 2009. Temporal changes of surface wave velocity associated with major Sumatra earthquakes from ambient noise correlation, *Proc. Natl. Acad. Sci. USA,* **106**(34), 14 207–14 212.

Yates, A., 2018. Seismic velocity changes at White Island volcano, New Zealand, using ten years of ambient noise interferometry, *MSc thesis*, Victoria University of Wellington.

Yates, A.S., Savage, M.K., Jolly, A.D., Caudron, C. & Hamling, I.J., 2019. Volcanic, coseismic, and seasonal changes detected at White Island (Whakaari) volcano, New Zealand, using seismic ambient noise, *Geophys. Res. Lett.,* **46**(1), 99–108.

Yuan, C., Bryan, J. & Denolle, M., 2021. Numerical comparison of time-, frequency- and wavelet-domain methods for coda wave interferometry, *Geophys. J. Int.*, **226**(2), 828–846.

SUPPORTING INFORMATION

Supplementary data are available at *GJI* online.

Supplementary Text section 9.1. Calculation of SNR and determination of the best analysis parameters.
Supplementary Text section 9.2. Velocity Change Calculations.
Figure S1. DPRI station availability. Stations are listed along the left with dates along the bottom. Coloured bars indicate availability for different components: yellow, east; green, north; blue, vertical. The box below shows when and how many stations are operating. Green lines show large-magnitude ($M_w > 5.6$) earthquakes and the pink line shows the Kaikōura earthquake.
Figure S2. Spectrogram for station MLF showing energy at different frequencies with the time in seconds since the beginning of the day for 2016 November 16. (a) Earthquake waveform with the earthquake signal in the middle and background noise before and after. (b) Spectrogram showing the frequency of the earthquake signal as well as faint background noise at low frequencies in the red box. (c) Background noise. Energy primarily in frequency range 0.01–1.2 Hz.
Figure S3. Velocity changes using a 6 month and a 2-yr reference period for the vertical–vertical component pairs for different moving stack lengths (5, 10, 20 and 30 d). The pink line shows the 2016 Kaikōura earthquake.
Figure S4. Velocity changes for the vertical–vertical component for 5-, 10-, 20- and 30-d moving stack lengths using a 6-yr reference period, smoothed with a 30-d moving average window (rolling). The green lines indicate large-magnitude earthquakes ($M_w > 5.6$) that occurred in this time period. The 2016 Kaikōura earthquake is shown by the pink line.
Figure S5. Correlation coefficient plot showing a good result from station pair SJQ–WJM with a 0.1–0.9 Hz filter. This was generated using the 2-yr test and started on 2016 January 1 and ended on 2018 February 28. The decrease in September 2016 is a result of a lack of data at both stations SJQ and WJM (Fig. S1). The pink line shows the 2016 Kaikōura earthquake.
Figure S6. Correlation coefficient plot showing a poor result from station pair CCB–CVR with a 0.1–0.9 Hz filter. This was generated using the 2-yr test and started on 2016 January 1 and ended prior to the Kaikōura earthquake due to a lack of data (Fig. S1). The pink line shows the 2016 Kaikōura earthquake.
Figure S7. Plot demonstrating how the $\delta v/v$ change following the earthquake was calculated at each station pair (ZZ component). Using $\delta v/v$ measurements from 30-d stacks (vertical component station pairs), smoothed with a 10-d moving median (rolling), the pre-earthquake measurement of dv/v is made by taking an average $\delta v/v$ within a 10-d window (blue bar) prior to the earthquake (red bar). A second 10-d window is used for post-earthquake $\delta v/v$, and the difference between the two windows is calculated for final $\delta v/v$ change. The position of the second window is chosen to take into account the 30-d stack size, ensuring all days within the window are using cross-correlation functions computed using post-earthquake data. For some station pairs, data issues meant the second measurement needed to be made at a later time. See Table S6 for full measurement details.
Figure S8. Lag time dependence on $\delta v/v$ for station pair IKR–MLF. Top: $\delta v/v$ computed using different lag times, smoothed with 10-d moving median (rolling), colour coded by key in bottom plot. Blue bars indicate where the value of velocity change is recorded (averaged over 10 d), with the difference then used to record the co-seismic velocity change. The position of the second window is chosen taking into account a stack size of 30 d, ensuring only post-earthquake cross-correlation functions are included in the measurement. Bottom: measurements of velocity change against central lag time of coda window used.
Figure S9. Plot of inverted single-station $\delta v/v$ against simulated PGV, and corresponding forward modelled station pair $\delta v/v$ compared to observed $\delta v/v$ for: (a and b) only station pairs that allowed immediate measurement following the earthquake (same as Figs 7b and c) and (c and d) the same station pairs as (a) and (b), but now additionally including all station pairs that use station SVR (regardless of timing of measurement). This is done for the purpose of checking the robustness of anomalous $\delta v/v$ estimated at station SVR, where only one station pair that used SVR station is included in initial inversion shown in (a) and (b) compared to four station pairs using SVR station in (c) and (d). SVR is still estimated to have experienced only a small change in $\delta v/v$ following the earthquake after further station pairs are included, with the modelled $\delta v/v$ still closely fitting the observed $\delta v/v$.
Figure S10. PGV measured for earthquakes listed in Table S2, as recorded by strong motion GeoNet sensor MOLS. For each event, we record the maximum velocity for each horizontal component (red circles) and select the maximum of these to provide an estimate of the PGV for the events in the region containing seismic stations used in this study. Waveforms follow order in Table S2.
Figure S11. PGV measured for earthquakes listed in Table S2, as recorded by strong motion GeoNet sensor WTMC. For each event, we record the maximum velocity for each horizontal component (red circles) and select the maximum of these to provide an estimate of the PGV for the events in the region containing seismic stations used in this study. Waveforms follow order in Table S2.
Figure S12. Coherent energy is observed for all nine component pairs by plotting the SNR versus lag-time for a 30-d cross-correlation function. Different coloured lines indicate different component pairs. All component pairs show peaks at both negative and positive lag times. Component pairs NN, NZ and ZN show a smaller peak at a negative lag time than other component pairs. These station pairs were used as only these pairs contained data consistently for 30 d to produce SNR values. To produce an SNR plot displaying different component pairs with a consistent stack size (30 d), all station pairs had to have no gaps in days greater than the stack size used. As a result of station outages (Fig. S1) and different stations being available for different component pairs, different station pairs were used to show an SNR result for each component pair. Also due to these large gaps, smaller stack sizes (20 d) were difficult to compute SNR results from. This shows energy travelling between stations as peaks are observed at positive and negative lag times for all component pairs.
Figure S13. Moving-window cross-spectral analysis example for station pair SJQ–WJM on 2016 December 31, with both forced (in black) and unforced linear regression (in red) with dashed lines showing the standard error for both, calculated from squared misfit of the modelled slope of the phase displacement. In this example, a velocity lag of 1 km s^{-1} was used, where the interstation distance for this pair is 23 km. Delay times used to calculate the slope are coloured blue while those that fall outside the windows are coloured red. These are weighted by the cross-spectral coherence and depend

on four factors: minimum and maximum lag-time, maximum delay time, maximum error and minimum coherence. Green boxes correspond to minimum and maximum lag times at positive and negative lags.

Table S1. Station locations.

Table S2. Table describing the numbers annotating earthquakes in Fig. 1. Earthquake information such as magnitude, latitude and longitude, and depth are obtained from GNS Science. Estimates of PGV in the study region are made using horizontal components from strong motion sensors MOLS and WTMC (Figs S10 and S11). Location of these strong motion sensors can be seen in Fig. 1.

Table S3. Station pair pre-processing parameters (MSNoise Version 1.5). These are the parameters used to process raw ambient noise data through to velocity.

Table S4. Station pair data set filter table (MSNoise Version 1.5).

Table S5. Frequently referenced previous studies.

Table S6. Details of $\delta v/v$ measurements made pre- and post- earthquake using the approach detailed in Fig. S7. The time window used to measure pre-earthquake $\delta v/v$ is defined by columns 'preEQ start' and 'preEQ end', and the window used to measure post-earthquake $\delta v/v$ defined by columns 'postEQ start' and 'postEQ end'.